Effects of forcing time scale on the simulated turbulent flows and turbulent collision statistics of inertial particles

B. Rosa, H. Parishani, O. Ayala, and L.-P. Wang

Articles you may be interested in

Guidelines for the formulation of Lagrangian stochastic models for particle simulations of single-phase and dispersed two-phase turbulent flows
Phys. Fluids **26**, 113303 (2014); 10.1063/1.4901315

Simulation of a particle-laden turbulent channel flow using an improved stochastic Lagrangian model
Phys. Fluids **21**, 043303 (2009); 10.1063/1.3115056

On the simulation of particle trajectories in turbulent flows
Phys. Fluids **16**, 4353 (2004); 10.1063/1.1804551

Optimal large eddy simulation of turbulent channel flow based on direct numerical simulation statistical data
Phys. Fluids **14**, 3675 (2002); 10.1063/1.1503803

Stochastic simulation of heavy-particle trajectories in turbulent flows
Phys. Fluids **14**, 342 (2002); 10.1063/1.1426392

Effects of forcing time scale on the simulated turbulent flows and turbulent collision statistics of inertial particles

B. Rosa,[1,a)] H. Parishani,[2,3] O. Ayala,[4] and L.-P. Wang[2,5]

[1]*Institute of Meteorology and Water Management - National Research Institute, 61 Podlesna Street, 01-673 Warsaw, Poland*
[2]*Department of Mechanical Engineering, University of Delaware, Newark, Delaware 19716-3140, USA*
[3]*Department of Earth System Science, University of California, Irvine, California 92697-3100, USA*
[4]*Department of Engineering Technology, Old Dominion University, 214 Kaufman Hall, Norfolk, Virginia 23529, USA*
[5]*The State Key Laboratory of Coal Combustion, Huazhong University of Science and Technology, Wuhan 430074, People's Republic of China*

In this paper, we study systematically the effects of forcing time scale in the large-scale stochastic forcing scheme of Eswaran and Pope ["An examination of forcing in direct numerical simulations of turbulence," Comput. Fluids **16**, 257 (1988)] on the simulated flow structures and statistics of forced turbulence. Using direct numerical simulations, we find that the forcing time scale affects the flow dissipation rate and flow Reynolds number. Other flow statistics can be predicted using the altered flow dissipation rate and flow Reynolds number, except when the forcing time scale is made unrealistically large to yield a Taylor microscale flow Reynolds number of 30 and less. We then study the effects of forcing time scale on the kinematic collision statistics of inertial particles. We show that the radial distribution function and the radial relative velocity may depend on the forcing time scale when it becomes comparable to the eddy turnover time. This dependence, however, can be largely explained in terms of altered flow Reynolds number and the changing range of flow length scales present in the turbulent flow. We argue that removing this dependence is important when studying the Reynolds number dependence of the turbulent collision statistics. The results are also compared to those based on a deterministic forcing scheme to better understand the role of large-scale forcing, relative to that of the small-scale turbulence, on turbulent collision of inertial particles. To further elucidate the correlation between the altered flow structures and dynamics of inertial particles, a conditional analysis has been performed, showing that the regions of higher collision rate of inertial particles are well correlated with the regions of lower vorticity. Regions of higher concentration of pairs at contact are found to be highly correlated with the region of high energy dissipation rate. © *2015 AIP Publishing LLC.* [http://dx.doi.org/10.1063/1.4906334]

I. INTRODUCTION

In recent years, a homogeneous and isotropic turbulence (HIT) simulated by the pseudo-spectral algorithm has been widely used to study statistics, structure, and dynamics of small-scale turbulence and dynamics of suspended inertial particles under the one-way coupling and two-way coupling.[1] Such simulations have been used to address a number of applications ranging from turbulent collision of cloud droplets,[2,3] clustering of aerosol particles,[4] combustion processes,[5] and scalar transport.[6,7]

a)Electronic mail: bogdan.rosa@imgw.pl

27, 015105-1

The main advantage of the pseudo-spectral approach is the spectral accuracy. HIT makes use of periodic boundary conditions and can be made statistically stationary by employing a large-scale forcing, where the kinetic energy is continuously injected into the large scales of the flow. Restricting the forcing to large scales only is thought to ensure that the small scales of the flow are unaffected by the forcing.[8] However, in the pseudo-spectral simulations, the dynamics at small scales may be affected by the numerical method for reducing the "aliasing" error.[9] The large-scale forcing is most cleanly done in the Fourier space, which can be conveniently integrated into the pseudo-spectral approach.

The large-scale forcing can be either deterministic[10,11] or stochastic.[12] In this study, we focus mainly on the stochastic method developed by Eswaran and Pope.[12] This forcing was carefully designed to ensure a statistically stationary turbulence is maintained at every time instant. It has been employed in a large number of direct numerical simulations of homogeneous isotropic turbulence and related simulations of turbulent particle-laden flows. An important parameter of this scheme is the forcing time scale. Its value is typically made much smaller than the large-eddy turnover time but larger than the time step, in order to generate a desired energy dissipation rate. One may argue that different forcing time scales relative to the flow physical time scales could be used to represent different mechanisms of the energy input. For example, a short forcing time scale mimics random energy input, while a forcing time scale comparable to the flow integral time scale could be viewed as an energy transfer from larger scales that are not included in the simulation. In this sense, different choices of the forcing time are physically meaningful. However, the implications of different treatments are not fully understood. In their original paper, Eswaran and Pope[12] showed the impact of forcing time scale on the simulated turbulence, but their work was limited to low flow Reynolds numbers at that time. We found recently that the ratio of the forcing time scale to the Kolmogorov time could affect the statistics and structure of the simulated flow as well as the dynamics and collision statistics of inertial particles. We note that typical deterministic forcing methods add energy at the time scale corresponding to the integral time scale of the flow, as implied by the dynamics of the large-scale flow field.

In this study, we conduct a thorough and systematic investigation, by means of direct numerical simulations (DNS), of the effects of forcing time scale on both the characteristics of simulated HIT and collision statistics of suspended inertial particles. The dynamics of an inertial particle depend on its own inertial response time, or more precisely, the ratio of the inertial response time to the characteristic time scales of the flow.[13] It is important to understand any effect of the forcing time scale as this also represents a time scale (although somewhat artificial) that is being introduced into the flow, and to be able to interpret such resulting effects.

The paper is organized as follows. In Sec. II, we describe briefly the essential details of the relevant numerical method and the stochastic forcing scheme. In Sec. III, a wide range of forcing time scales (compared to the time step size, Kolmogorov time, and integral time) will be considered and the simulated flow statistics will be compared and interpreted. The resulting collision statistics for suspended inertial particles will also be analyzed and interpreted in Secs. IV and V. Section VI contains a summary and main conclusions.

II. THE NUMERICAL METHOD

We consider simulations of forced HIT and collision statistics of suspended inertial particles. The details and the most recent implementation have been summarized by Rosa *et al.*,[1] along with a parallel implementation method based on two-dimensional domain decomposition. Under the conditions that the particle to fluid density ratio is high ($\sim 10^3$), the particle volume fraction is low (10^{-5} or less), and the particle diameter d_p is much smaller than the flow Kolmogorov length η ($d_p/\eta < 0.1$), it is assumed that the background turbulence is not affected by the suspended particles. In this study, particle-particle local hydrodynamic interactions[14] will not be considered.

The fluid flow is simulated by a standard pseudo-spectral method,[15] which solves the Navier-Stokes equation on a 3D uniform mesh with N equally spaced grid points in each spatial direction. The motion of a large number of inertial particles is followed by a Lagrangian approach. Particle tracking and collision detection are handled by a specially designed parallel algorithm with

optimized data communication between processes. The algorithm employs the cell-index method and the concept of linked lists[16] for efficient detection of closely spaced particles. The fluid solver utilizes an efficient 3D fast Fourier transform (FFT).[17] The new FFT is based on 2D domain decomposition of 3D data field and a sequence of 1D FFT from the FFTW library (www.fftw.org) in each spatial direction. The approach provides an optimal balance between computation and communication on a scalable computer with O(10 000) to O(100 000) processors. The code is designed mainly to run on supercomputers with distributed memory. For data communication, the standard MPI (Message Passing Interface) library is used. A complete description of the code together with results of numerical experiments and scalability analysis can be found in study by Ayala *et al.*[18]

The first step in the simulation is to develop a homogenous isotropic turbulent flow in a cubic domain of size $(2\pi)^3$. The incompressible Navier-Stokes (N-S) equations,

$$\frac{\partial \mathbf{U}}{\partial t} = \mathbf{U} \times \omega - \nabla\Big(\frac{P}{\rho} + \frac{1}{2}\mathbf{U}^2\Big) + \nu\nabla^2\mathbf{U} + \mathbf{f}(\mathbf{x},t), \tag{1}$$

$$\nabla \cdot \mathbf{U}(\mathbf{x},t) = 0, \tag{2}$$

are solved by applying periodic boundary conditions in all the three directions. Here, $\omega \equiv \nabla \times \mathbf{U}$ is the vorticity vector, P is the pressure, ρ is fluid density, and ν is fluid kinematic viscosity (i.e., the air viscosity). For a given resolution (N) of the computational mesh, the viscosity is specified as

$$\nu \approx \frac{0.45}{(N/32)^{4/3}} \tag{3}$$

in the spectral units (meaning that the domain size is set to 2π in length). Such specification ensures that, on the one hand, the smallest scales are adequately resolved, and, on the other hand, a large flow Reynolds number can be obtained. In this paper, the viscosity is made to only depend on N.

In the pseudo-spectral method, the computation in the physical space of the nonlinear term in the Navier-Stokes equation introduces aliasing errors.[9] In an undealiased pseudo-spectral simulation, harmonic modes with wavenumbers above the largest resolved wavenumber may contaminate some of resolved modes. To partially remove the aliasing errors, high modes with wavenumber $|\mathbf{k}| \geq N/2 - 1.5$ are filtered.

The flow is driven by the forcing term $\mathbf{f}(\mathbf{x},t)$, which is nonzero only for the 80 low-wavenumber modes in the Fourier space ($|\mathbf{k}| < \sqrt{8}$). The specification of the acceleration forcing is based on Uhlenbeck-Ornstein random processes.[12] In the spectral space, the forcing term $\hat{\mathbf{f}}(\mathbf{k},t)$ is defined as

$$\hat{\mathbf{f}}(\mathbf{k},t) = \sum_{j=1}^{3} A_j(\mathbf{k},t)e^{2\pi i r(\mathbf{k},t,j)}, \tag{4}$$

where r is a random real number in the range of [0, 1]. The amplitude $A_j(\mathbf{k},t)$ is a function of an acceleration variance σ_f^2, forcing time scale t_f, integration time step Δt, and a second independent random number θ in the range of [0, 1]

$$A_j(\mathbf{k},t) = \sqrt{\frac{-4\sigma_f^2 \ln\theta(\mathbf{k},t,j)\Delta t}{t_f}}. \tag{5}$$

The continuity condition $\mathbf{k} \cdot \hat{\mathbf{f}}(\mathbf{k},t) = 0$ is forced by taking the projection onto the plane normal to $\mathbf{k}$. To conclude, there are two characteristic input parameters defining the stochastic forcing scheme, namely, the acceleration variance σ_f^2 and forcing time scale t_f. The time scale t_f is typically made smaller than the eddy turnover time T_e, otherwise the stochastic forcing may become correlated with the flow, and the level of energy input will be reduced. Eswaran and Pope[12] showed that the average rate of energy input (which is also the average dissipation rate for a statistically stationary turbulence) could be expressed as

$$\epsilon = 4N_f\sigma_f^2 t_f \times \frac{1}{1 + t_f(\sigma_f^2 t_f N_f k_0^2)^{1/3}/\beta}, \tag{6}$$

where the number of modes being forced is $N_f = 80$, the lowest wavenumber is $k_0 = 1$, and the fitting coefficient β was found to be 0.8. In all performed simulations at different grid resolutions,

we kept the reference dissipation rate $\epsilon_0 = 4N_f\sigma_f^2 t_f$, at $\epsilon_0 = 3600$. Having established the values of the viscosity ν and the forcing parameter ϵ_0, we then define t_f and σ_f^2 as

$$t_f = t^*\sqrt{\frac{\nu}{\epsilon_0}}, \qquad \sigma_f^2 = \frac{\epsilon_0}{4N_f t_f}. \tag{7}$$

Namely, we have transformed the raw input parameters N, σ_f^2, and t_f to three input parameters N, σ_f^2, and t^*. In our simulations, t^* is in the range of 0.01–10 000. It should be noted that a change in the time scale results also in the change of the acceleration variance σ_f^2. The above settings are designed to yield roughly $t_f/\tau_K = t^*$ when t^* is small, as in this limit the actual flow dissipation rate is the same as ϵ_0. If t^* is not small, then the realized dissipation rate will be less than ϵ_0 and consequently $t_f/\tau_K < t^*$. In the analysis and interpretation of the flow to be presented later in the paper, we further transform the specification of the flow in terms of three independent parameters: the viscosity ν, the actual realized average flow dissipation rate ϵ, and the Taylor-microscale flow Reynolds number R_λ. Other combinations of three parameters may occasionally be used in some plots. These different choices of problem specification are all equivalent.

To initialize the velocity field, we used a random phase algorithm with a prescribed Kolmogorov energy spectrum as $E(k) \propto |\mathbf{k}|^{-5/3}$.[19] However, the stationary flow field does not depend on this initial energy spectrum. The initial spectrum only affects the transition time from the initial flow to the stationary flow.

Once the background turbulent velocity field $\mathbf{U}(\mathbf{X}, t)$ is established, inertial particles are advanced by solving their equation of motion[20] including particle inertia, viscous drag, and the body force

$$\frac{d\mathbf{V}^{(k)}(t)}{dt} = -\frac{\mathbf{V}^{(k)}(t) - \mathbf{U}(\mathbf{Y}^{(k)}(t), t)}{\tau_p^{(k)}} + \mathbf{g}, \tag{8}$$

$$\frac{d\mathbf{Y}^{(k)}(t)}{dt} = \mathbf{V}^{(k)}(t), \tag{9}$$

where k is the particle number, $\tau_p^{(k)}$ is the Stokes inertial response time, $\mathbf{V}^{(k)}(t)$ is actual particle velocity, $\mathbf{U}(\mathbf{Y}^{(k)}(t), t)$ denotes the fluid velocity at the actual particle location $\mathbf{Y}^{(k)}(t)$, and $\mathbf{g}$ is the gravitational acceleration. Particles are initially introduced to the flow at random locations. In this study, we focus on inertial particles relevant to cloud droplets of radius from 10 to 60 μm. For such particles, the Reynolds number is of the order 1 or less, and the Stokes drag is assumed. Since our study was motivated by the growth of cloud droplets due to collision-coalescence which is primarily governed by differential sedimentation, the gravity force must be included in the droplet equation of motion. In the present simulations, droplets were allowed to overlap and move independently, namely, they were treated as ghost particles.

III. RESULTS ON FLOW STATISTICS

We shall first discuss and analyze the structure and statistics of the simulated turbulent flows. In Figure 1, we present visualizations of instantaneous vorticity fields during the stationary stage, obtained using four different forcing time scales. Flows simulated with shorter time scales, namely, $t^* < 1$ all resemble the flow with $t^* = 1$ in Figure 1.

Each simulation was performed at the grid resolution of 128^3 with the same time step size. The figure provides qualitative insight into the structures of the flows and clearly illustrates how the characteristic features of the flow depend on t^*. Shorter forcing time scale results in finer vortical structures and higher density of the structures. The size of eddies grows with the forcing time scale. It is also worth emphasizing that a larger magnitude of the vorticity is observed in simulations with a shorter t_f. To quantify the effect of the forcing time scale on the vorticity field, two basic statistics have been computed. Table I shows maximum (ω_{max}) and mean ($\langle\omega\rangle$) values of the vorticity magnitude. The statistics were computed in eight simulations using different forcing time scales. Both quantities were averaged over 30 000 time steps. We conclude that, in the statistical sense, the
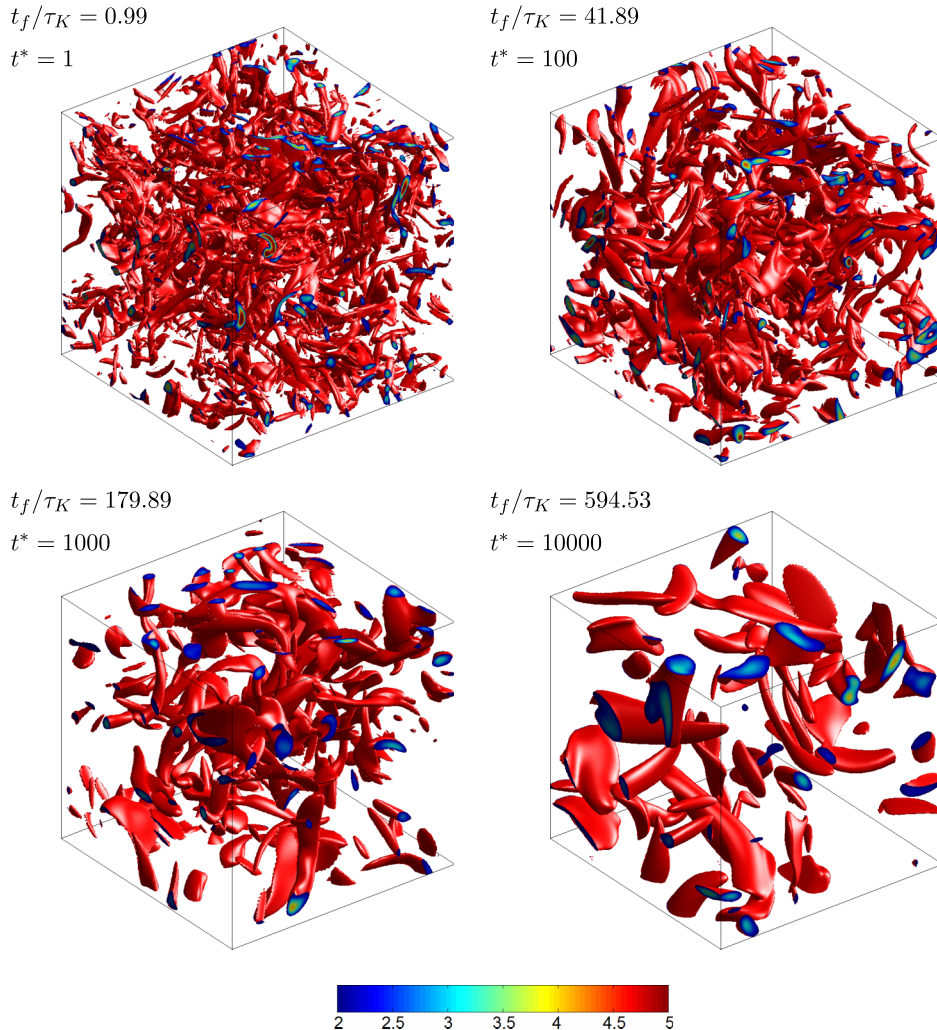
FIG. 1. Vorticity isosurfaces (in red) and vorticity magnitude inside vortex structures at the boundaries of the domain (shown with color mapping) for the simulated flows with different forcing time scales ($N = 128^3$). Red isosurfaces represent the magnitude at 2 times the local-in-time field mean. The color-map range is from 2 to 5 and corresponds to the actual value of vorticity normalized by the mean.

vorticity field does not change when $t_f < \tau_K$. The relative difference in $\langle \omega \rangle$, between flows forced with $t^* < 1$, is within statistical uncertainty.

Apart from the vortical tubes such as those shown in Figure 1, the turbulent flow contains also regions of high strain rate. The regions of high strain rate and low vorticity are typically the places

TABLE I. Statistics of vorticity field and their uncertainties in DNS units. ω_{max} refers to the maximum value of the vorticity magnitude while $\langle \omega \rangle$ represents the mean value averaged over 30 000 time steps. Each simulation was performed at the grid resolution of 128^3.

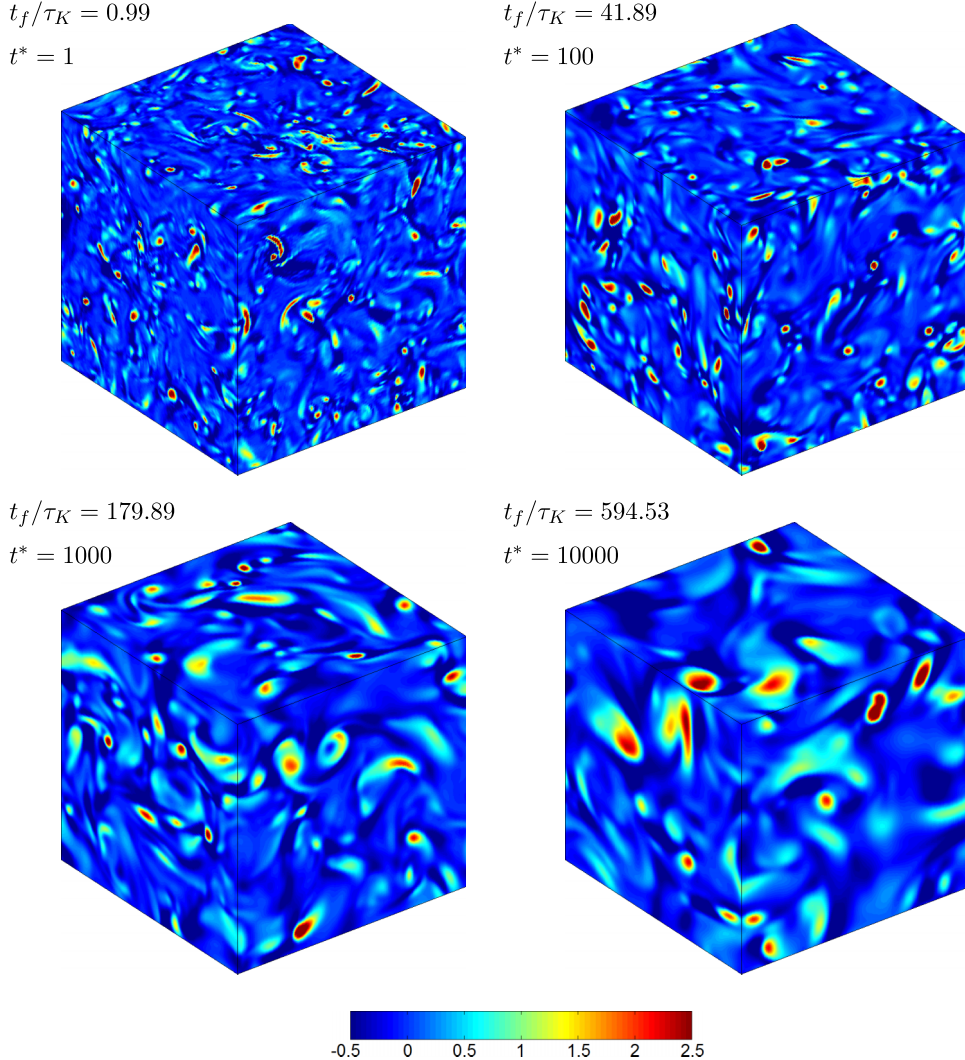| t^*	0.02	0.05	0.1	1	10	100	1000	10 000
ω_{max}	1916.5	1915.3	1918.9	1919.4	1587.9	751.9	238.9	73.8
$\delta\omega_{max}$	24.9	21.9	21.2	26.9	25.2	12.2	8.3	5.1
$\langle \omega \rangle$	179.1	179.3	179.1	181.0	146.1	79.6	33.3	12.5
$\delta\langle \omega \rangle$	2.3	2.7	1.8	3.0	1.9	0.9	0.7	0.2
$\omega_{max}/\langle \omega \rangle$	10.7	10.7	10.7	10.6	10.9	9.4	7.2	5.9

FIG. 2. Visualization of the second invariant of the velocity gradient tensor, normalized by its r.m.s. (local-in-time) value, on the boundaries of the domain. Different panels correspond to different forcing time scales. The snapshots presented here are for the same time instants used for the snapshots presented in Figure 1.

where heavy particles tend to cluster. To distinguish vortices from shear layers, an alternate quantity is considered. Figure 2 presents the second invariant of the deformation tensor II_2[21] normalized by its r.m.s. value. II_2 is defined as

$$II_2 = -\frac{1}{2}\frac{\partial u_i}{\partial x_j}\frac{\partial u_j}{\partial x_i} = \frac{1}{2}\left(\frac{\omega_i \omega_i}{2} - S_{ij}S_{ij}\right),\tag{10}$$

where S_{ij} is the rate of strain, and ω_i is the vorticity. Regions where II_2 is large and negative are regions of high strain rate. The regions where II_2 is large and positive are regions of high vorticity. This interpretation is consistent with the visualizations presented in Figure 2. The red areas indicate the location of the vortex tubes. Since Figures 1 and 2 show the same flows, we can observe correlations between the vorticity magnitude and II_2.

Figure 3 shows the probability density functions for the normalized vorticity. Different lines correspond to simulations with different time scales of the forcing scheme. We present only the results from simulations at the resolution of 512^3. Plots from lower resolutions show similar trends. The data for each case represent averages over 3000 time steps. Vorticity fields were collected after $10T_e$ (T_e is eddy turnover time), i.e., when turbulence is homogenous and statistically stationary.
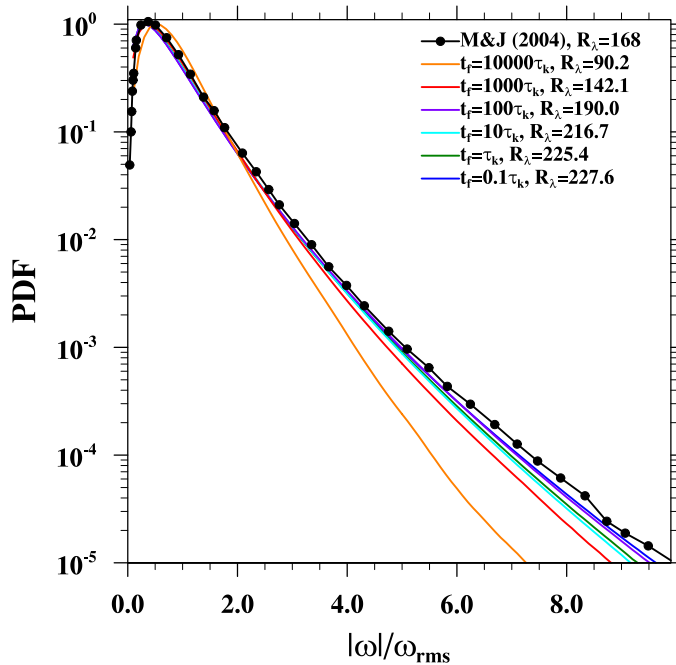
FIG. 3. Probability density function of the normalized vorticity from simulations at mesh sizes 512^3 with different t_f values.

Our results are compared with the DNS result of Moisy and Jimenez,[22] showing a remarkable agreement when the R_λ is comparable. The differences in the tail result mainly from different Reynolds numbers, with some minor effect of the different truncation radii in the dealiasing filter. Figure 3 shows also that the shorter the time scale, the more extended the tail is. Essentially, this is an effect of the flow Reynolds number as a shorter forcing time yields a larger flow Reynolds number. A large flow Reynolds number implies a wider scale separation between the large scales and the small scales, which is consistent to the smaller vortical structures seen in Figure 1 for smaller forcing time scale. There is clear evidence that the probability density function (PDF) curves converge as the flow Reynolds number is increased.

In Figure 4, we show the normalized energy spectra of the simulated flows at two different resolutions. The experimental data of grid-generated turbulence obtained by Comte-Bellot and Corrsin[23] are also shown for comparison. In the experiment,[23] the measurement station was located at $x/M = 98$, far from the turbulence-inducing grids, to ensure that the flow is homogenous and isotropic. The spectrum has been computed using the method described in Wang and Maxey,[24] i.e., by dividing the wavenumber space into $N/2$ shells of unit width according to the value of $|\mathbf{k}|$, and then summing the kinetic energy in each shell. Several important conclusions result from this comparison. First, in the inertial and dissipation ranges, energy spectra from the numerical simulations are in excellent agreement with the experimental spectrum. Second, the smallest scales being resolved for different values of t^* or t_f are different. For larger t_f, all scales are better resolved. At the same time, less large scales compared to the Kolmogorov scale are simulated. Third, for a given grid resolution, the spectra obtained with different t_f overlap except when t_f is too large leading to a too small R_λ.

The dissipation spectrum $D(k)$ is related to $E(k)$ by

$$D(k) = 2\nu k^2 E(k). \tag{11}$$

The dissipation rate decreases with the forcing time scale, but with Kolmogorov scaling, all the spectra collapse to one curve (see Figure 5) except the two cases of lowest R_λ. An interesting observation is that the position of the peak remains at $k\eta \approx 0.2$ for all cases.

Now we examine the key flow characteristics and their dependence on the forcing time scale. Presented in Figures 6–8 are the two statistics that determine the nature of the simulated turbulent flow. These are the average energy dissipation rate $\langle\epsilon\rangle$ (Figures 6 and 7) and Taylor microscale
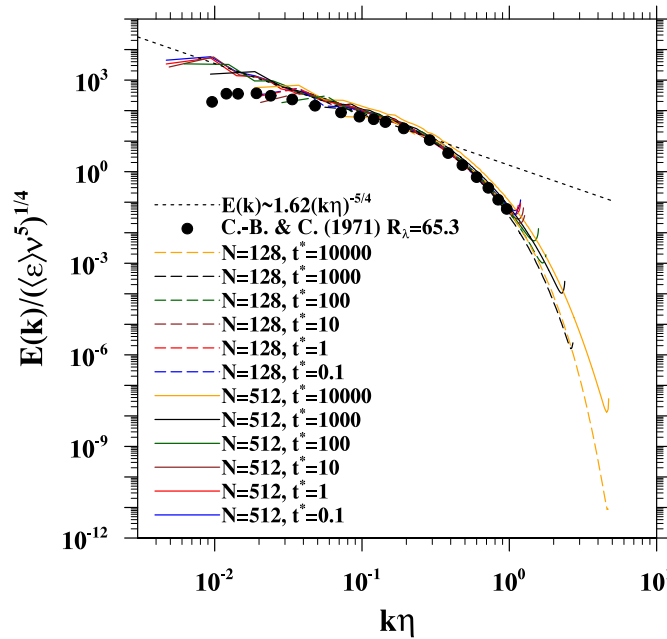
FIG. 4. The normalized energy spectra of the simulated flows at two different resolutions 128^3 (dashed lines) and 512^3 (solid lines). $\langle \epsilon \rangle$ is the average energy dissipation rate in the whole computational domain. The colors correspond to different forcing time scales. The experimental data[23] are plotted for comparison. Analytical representation for the inertial subrange[25] is plotted with a black dotted line.

Reynolds number (Figure 8) $R_\lambda = u'\lambda/\nu$ where u' is the r.m.s. fluctuating velocity and λ is the transverse Taylor microscale.

Energy dissipation rates are plotted in DNS units and are compared to the model Eq. (6). Several important conclusions can be drawn from Figures 6 and 7. First, energy dissipation rate is
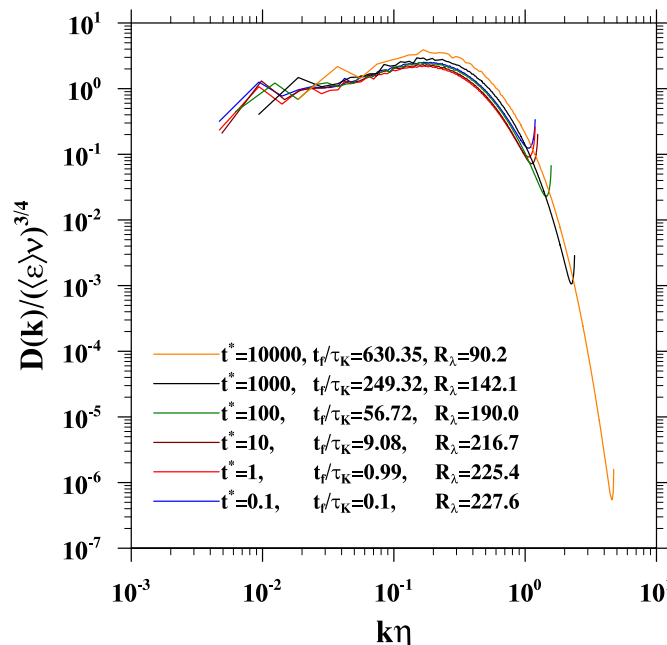
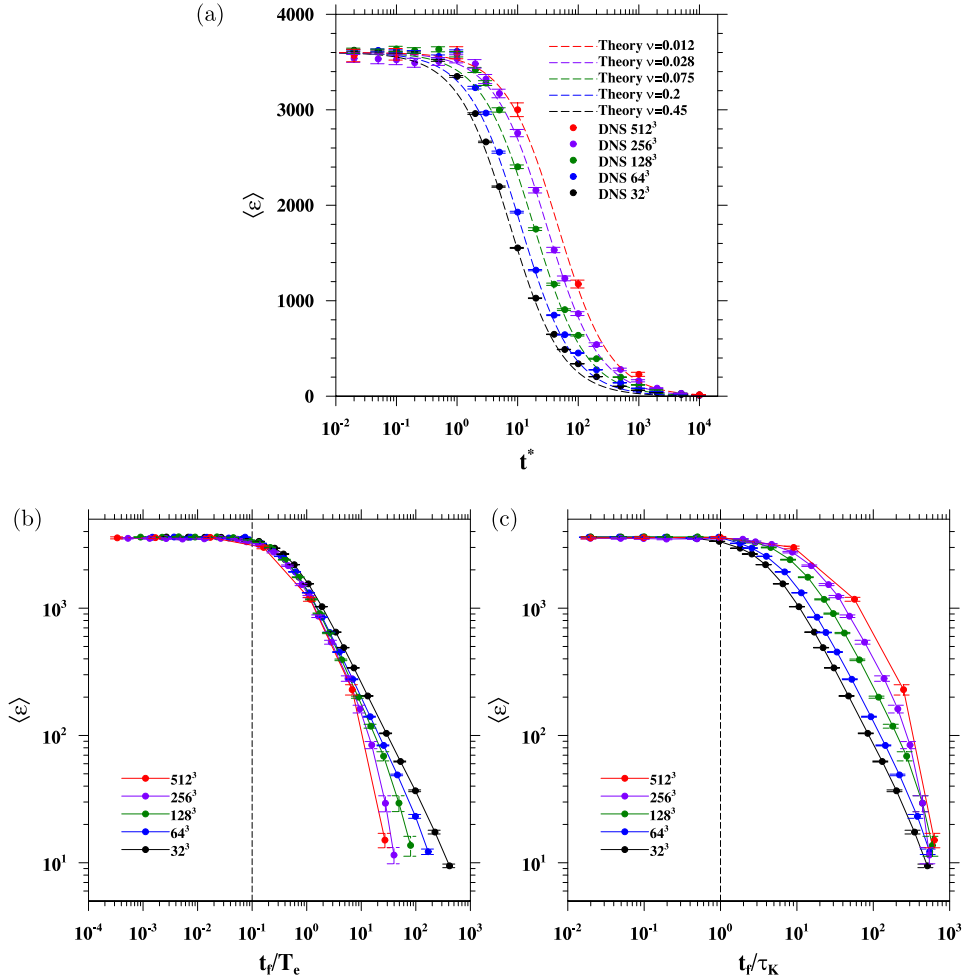FIG. 5. Normalized dissipation rate spectra.

FIG. 6. Panel (a) energy dissipation rates as function of t^*. The model predictions, Eq. (6), are also shown with $\beta = 0.8$. Panel (b) energy dissipation rate from DNS in log-log scale, with the x-axis being the forcing time scale Eq. (7) normalized by eddy turnover time. The vertical dashed line corresponds to $t_f = 0.1T_e$. Panel (c) $\langle \epsilon \rangle$ as in panel (b), with the x-axis being the forcing time scale normalized by the Kolmogorov time. The vertical dashed line corresponds to $t_f = t_K$.

not sensitive to forcing time scale if $t_f \leq \tau_K$, in agreement with the model prediction. Second, when $t_f > \tau_K$, the actual energy dissipation rate decreases with the forcing time scale, suggesting that less energy is supplied to the system. This observation confirms the theoretical model of Eswaran and Pope[12] that the energy-input rate tends to decrease with increasing t_f. The simulation results are in good agreement with the model. We confirmed that the fitting coefficient $\beta = 0.8$ gives fine prediction of expected energy dissipation rate in a wide range of forcing time scales. However, for $t^* = 1$, better agreement with DNS data is obtained with $\beta = 1.5$ (see Figure 7(b)). We note that actual dissipation rate depends on the grid size and is larger for higher resolutions.

Similarly to ϵ, the Taylor microscale Reynolds number is also not sensitive to forcing time scale (see Figure 8) if $t_f \leq \tau_K$. For larger t_f, R_λ decreases with the forcing time scale. This observation is consistent with qualitative information presented in Figure 1. By proper combinations of viscosity and forcing time scales, we are able to obtain the same R_λ at different grid resolutions. Figure 8(b) indicates that a turbulent flow with $R_\lambda = 120$ can be obtained from two different resolutions (256^3 and 512^3) by using different forcing times.

As indicated previously, the system can be described in terms of three parameters, and from now on, we will use ν, ϵ, and R_λ to describe other flow statistics. The Kolmogorov scales (η, τ_K, v_K) are determined only by ν and ϵ while $u' = 15^{-1/4}v_K R_\lambda^{1/2}$, $T_e = 15^{-1/2}\tau_K R_\lambda$, and $\lambda = 15^{1/4}\eta R_\lambda^{1/2}$.[26,27]
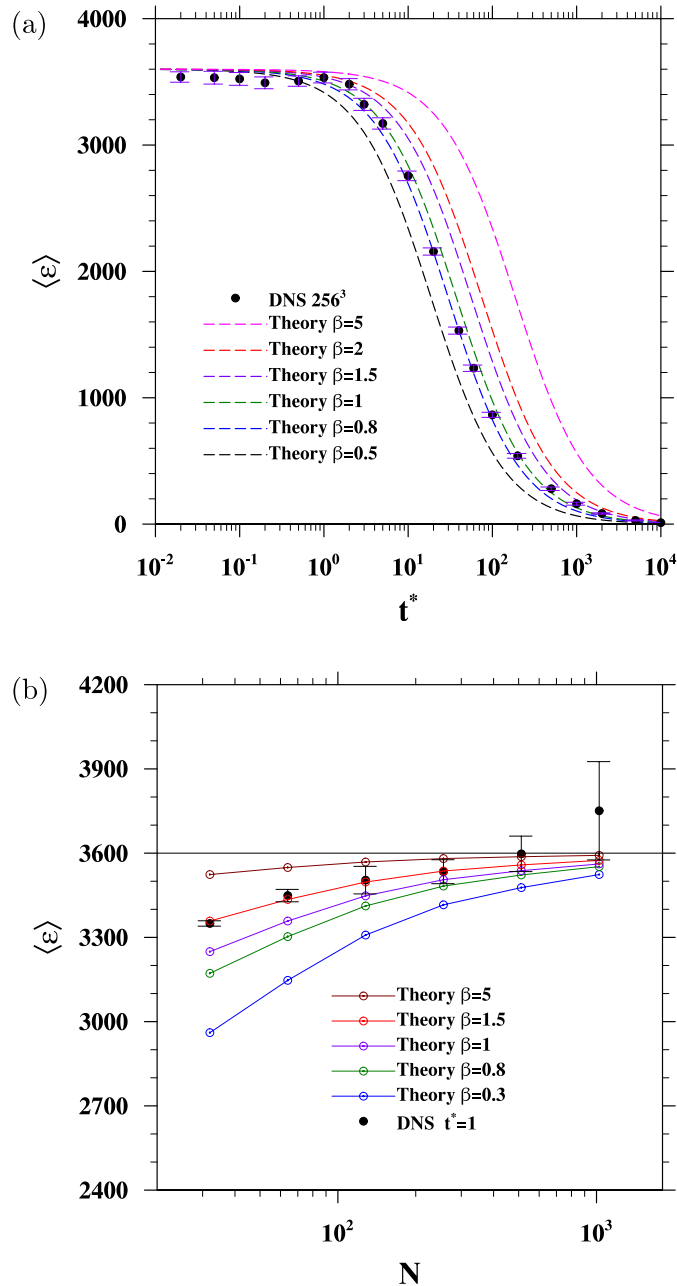
FIG. 7. Panel (a) energy dissipation rates as a function of t^*. Markers represent results from DNS at resolution N = 256. Dashed lines—model predictions (Eq. (6)) for different β values. Panel (b) energy dissipation rate from DNS (black markers) for $t^* = 1$ at different resolutions. Color lines represent analytical predictions Eq. (6).

An interesting question to pose is whether this set of parameters is complete or whether the forcing time scale also plays a role. As the forcing scheme mainly affects the large scales, the potential contribution from the scheme may appear in longitudinal integral length scale. In Figure 9, we present the normalized longitudinal integral length scale as a function of the forcing time scale normalized by the eddy turnover time. There are two interesting conclusions. First, in simulations at large resolution 512^3, the quantity remains constant for a wide range of forcing time scales. Second, in simulations at low resolutions, the normalized L_f does not change only when $t_f \leq \tau_K$ and then for larger t_f it rapidly increases. The slope of this increase depends on the resolution of computational grid.
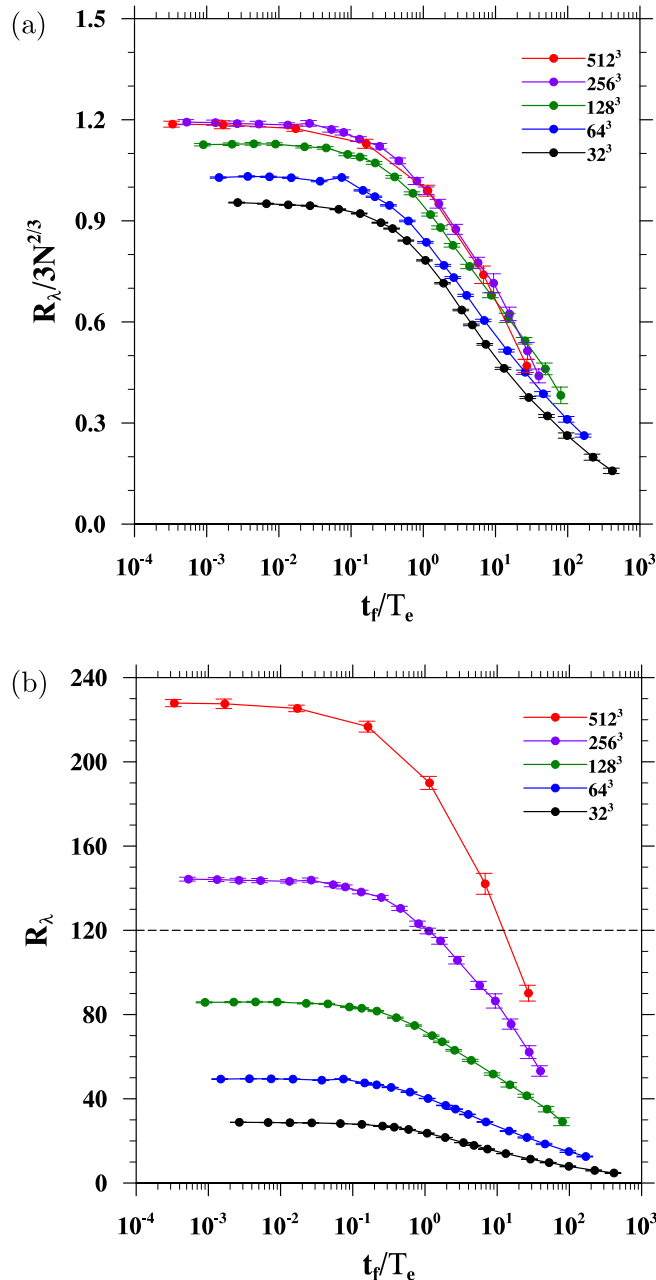
FIG. 8. (a) Taylor microscale Reynolds number normalized by $3N^{2/3}$ and (b) Taylor microscale Reynolds number as a function of forcing time scale.

Finally, we examine two dimensionless parameters: flatness (F) and skewness (S) of the longitudinal velocity gradient. The parameters characterize non-Gaussian and asymmetric behavior of the turbulence. Both were computed on the fly.[24] Figure 10(a) shows the flatness factor as a function of t^*. The characteristic feature of F is the monotonic dependence on the grid resolution or equivalently on the flow Reynolds number. It should be noted that in Figure 10(a), we have a double dependence of F on the R_λ. By changing forcing time scale, we change also R_λ. However, in both cases, the flatness factor is monotonic and increasing function of R_λ. Ishihara *et al.*[28] claimed that in the ordinary forced turbulence, the F factor monotonically increases as R_λ increases. Based on DNS results, they proposed an empirical formula that relates F with R_λ ($F \sim 1.14 R_\lambda^{0.34}$). Our numerical
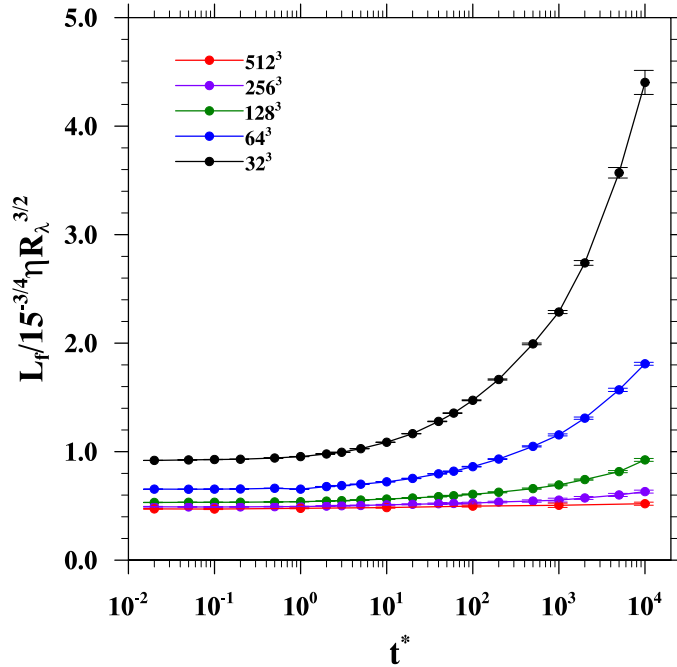
FIG. 9. Normalized longitudinal integral length scale plotted as a function of t^*.

results are consistent with their study. Figure 10(b) shows the normalized flatness factors computed in current simulations and normalized by analytic formula ($1.14R_\lambda^{0.34}$). For most simulations, except for those performed at small grid resolutions and large t^*, we observe good agreement between our DNS results and the empirical formula. It is worth noting that the sensitivity of the flatness factor on the forcing time scale depends on the grid resolution. For simulations performed at resolution 512^3, F is not sensitive to the forcing time scales if $t^* < 100$. For low resolution simulations (32^3), the dependence on the forcing time scale is observed already at $t^* = 10$.

A similar analysis has been performed for the skewness. Figure 11(a) shows the S factor as a function of t^*. In the current analysis, we refer again to the study by Ishihara *et al.*[28] They showed that skewness has a weaker dependence on the R_λ than flatness. Analytical formula for S, proposed in their study, is as follows $S \sim -0.32R_\lambda^{0.11}$. It implies that S monotonically decreases with
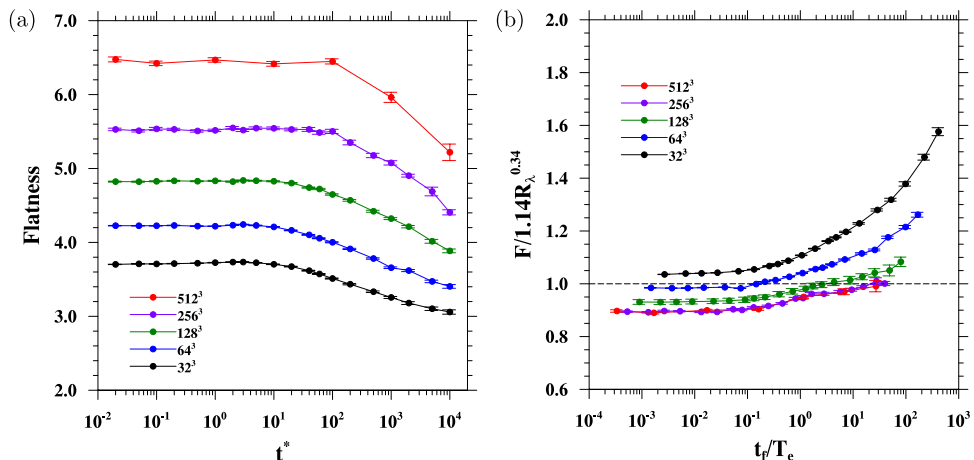

FIG. 10. (a) Flatness as a function of t^* and (b) flatness normalized by empirical formula of Ishihara *et al.*,[28] plotted as a function of the forcing time scale normalized by the eddy turnover time.
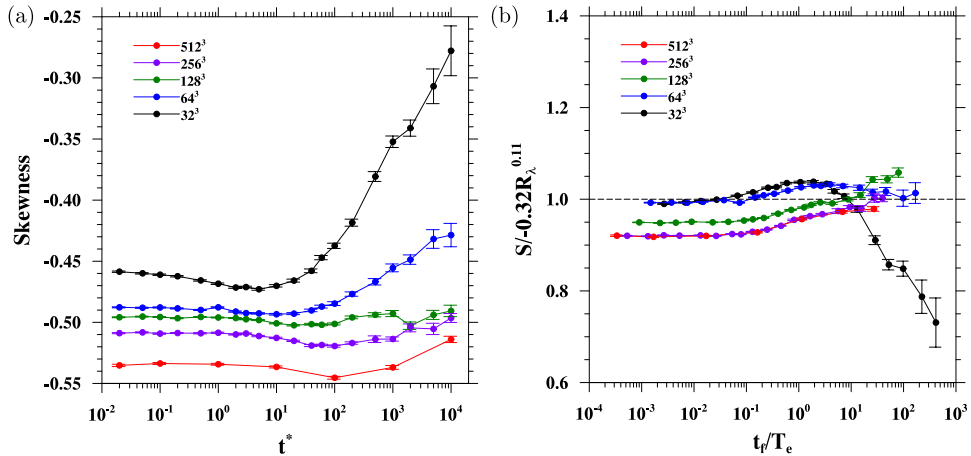
FIG. 11. (a) Skewness as a function of t^* and (b) skewness normalized by empirical formula of Ishihara *et al.*,[28] plotted as a function of the forcing time scale normalized by the eddy turnover time.

increasing R_λ. Our DNS results are in general agreement with the their findings. Figure 11(b) shows the skewness factor normalized by $-0.32R_\lambda^{0.11}$. For wide range of t^*, the normalized S is close to 1. Significant deviation is observed only in data computed in simulations at low resolution with forcing time scales $t^* > 100$. Since in this regime the domain is quite small and only large turbulent structures are present the deviation may result from too low the value of flow Reynolds number.

In Figures 6–10, the standard deviation $\sigma_{\overline{A}}$ of any given time-averaged quantity $\overline{A}$ has been calculated following Eswaran and Pope,[12] by $\sigma_{\overline{A}} = 2\sigma_A^2 T/\Delta T$, where $\overline{A}$ represents the time averaged value of A (where A is typically a volume-averaged quantity at a given time instant), T is the integral time scale of A, ΔT is the total time duration, and $\sigma_{\overline{A}}$ is the standard deviation of A. The integral time scale T was estimated by the time delay when the autocorrelation coefficient of the quantity takes a value of 0.5.

IV. KINEMATIC AND DYNAMIC STATISTICS FOR INERTIAL PARTICLES

In the second part of this study, we examine the impact of the forcing time scale on the geometric collision statistics of inertial particles. We focus on particles relevant to cloud droplets of radius from 10 to 60 μm. Therefore, in all simulations, gravity ($g = 9.8$ m/s) is included. The effects of gravity on the kinematic and dynamic statistics and on the acceleration and pair statistics have been carefully investigated in our recent studies.[1,29] The physical flow dissipation rate is assumed to be 400 cm^2/s^3 with physical viscosity set to that of the air. These are used to scale the DNS units to match the conditions of cloud droplets, as explained by Ayala *et al.*[30] Under these physical conditions, the Stokes number defined as the ratio of the particle's inertial response time to the Kolmogorov time $St = \tau_p/\tau_K$ varies from 0.063 to 2.28 and the velocity ratio $S_v = v_p/v_K$ from 0.446 to 16.1. Detailed dimensionless parameters are given in Table II. The inertial particles considered here have significant inertia relative to the Kolmogorov time thus may experience significant clustering. However, their inertia is not significant when compared to the large turbulence eddies.

The first quantity examined here is the monodisperse radial distribution function RDF(r) at contact ($r = 2a$).[30,31] The RDF is a measure of the effect of preferential concentration of droplets on the collision rate. Preferential concentration refers to the tendency of particles to accumulate in regions of the flow associated with, for example, high flow strain rate or low flow vorticity.[24] Figures 12, 13, and 14 show how the accumulation of inertial particles depends on the characteristic features of the turbulent flow and the Stokes number, these figures correspond to droplets of radius a = 20, 30, and 50 μm, respectively. The snapshots presented in subsequent panels (a)-(d) illustrate the distribution of particles suspended in flows forced with different time scales and having different R_λ. All simulations have been performed at the same resolution of the computational grid ($N = 128$). Since the values of

TABLE II. Basic properties of cloud droplets. (*) Based on DNS simulations at $N = 128$ with $t^* = 1$.

a (μm)	St	Sv	a/η	τ_p/T_e^*
10	0.063	0.446	0.017	0.0029
15	0.143	1.004	0.025	0.0065
20	0.254	1.784	0.034	0.0115
22.5	0.321	2.258	0.038	0.0146
27.5	0.480	3.374	0.046	0.0218
30	0.571	4.015	0.051	0.0260
40	1.015	7.138	0.068	0.0462
50	1.585	11.153	0.084	0.0722
60	2.283	16.060	0.101	0.1039
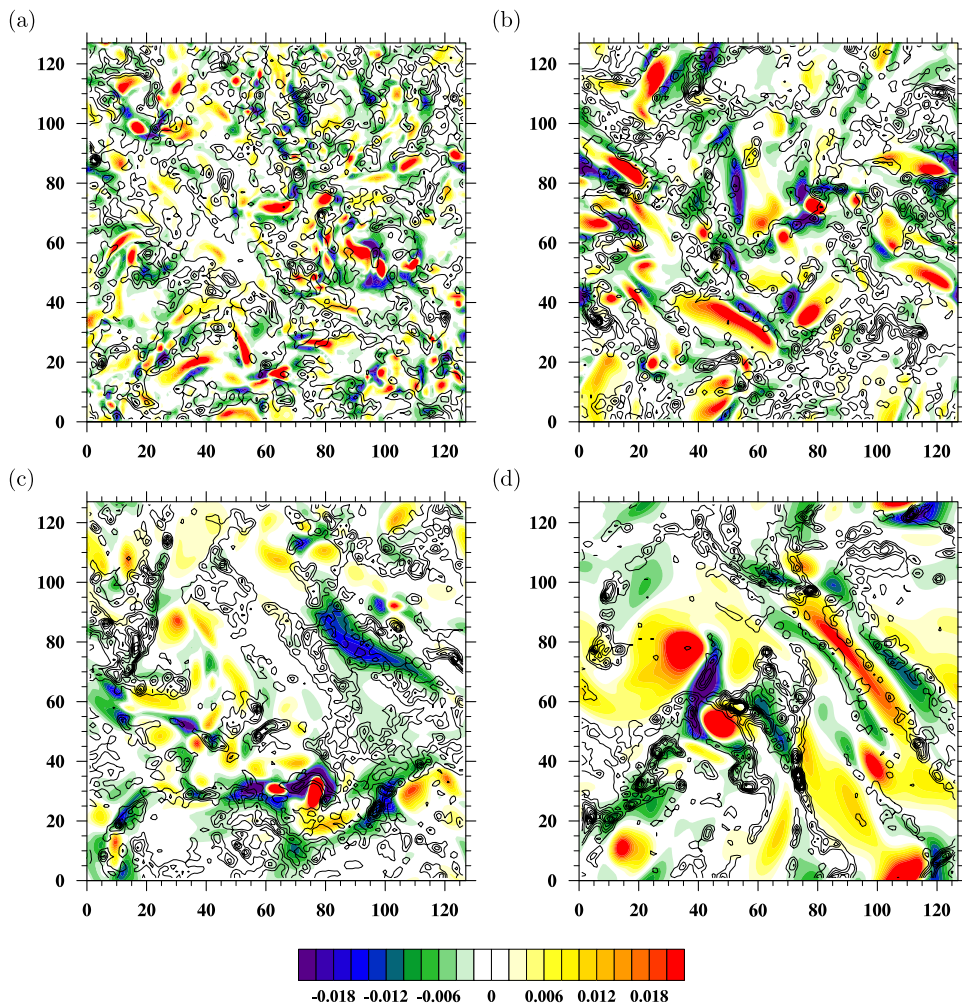
FIG. 12. Distributions of particles with Stokes number of 0.254 (droplet radius a = 20 μm) and the second invariant in a two-dimensional horizontal cross-section of the computational domain. Color indicates the field of the second invariant of the deformation tensor II_2 normalized by its r.m.s. value. Contour lines show particle concentration field (defined as the number of particle per grid cell, smoothed using a 3×3 point horizontal filter) using 0.25 as interval. All particles from two grid cell layers adjacent to the II_2 plane are included. Different panels correspond to simulations performed with different forcing time scales (a) $t^* = 1$, (b) $t^* = 100$, (c) $t^* = 1000$, and (d) $t^* = 10\,000$.
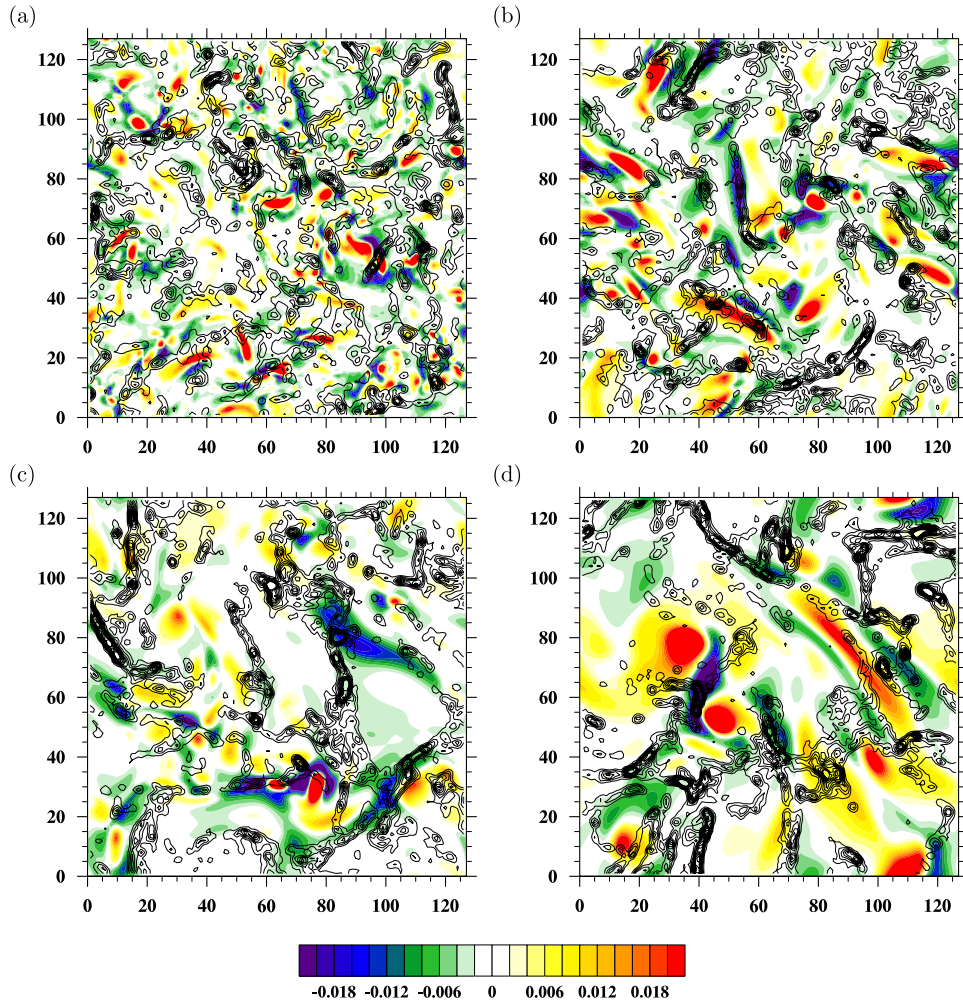
FIG. 13. Same as in Figure 12 but for particles with Stokes number 0.571 (droplet radius a = 30 μm). Different panels correspond to simulations performed with different forcing time scales (a) $t^* = 1$, (b) $t^* = 100$, (c) $t^* = 1000$, and (d) $t^* = 10\,000$.

Stokes number are on the order of one, significant preferential accumulation can be observed. Based on these plots, two general conclusions can be drawn. First, the length scale of the particle accumulation changes with the forcing time scale, due to the increase in the size of the Kolmogorov eddies when the forcing time scale is increased. Second, the droplets with larger inertia (50 μm) form more non-uniform structures than droplets with lower inertia (20 μm or 30 μm). We must note that both particle inertia and gravitational sedimentation affect the level of particle accumulation, as shown, for example, by Woittiez et al.,[32] Rosa et al.,[1] and Park and Lee.[33] Under certain combination of inertia and sedimentation, droplets form vertical bands of high concentration,[33] which can be observed in Fig. 15, where visualizations on a vertical slice are shown. This explains why the strongest overall accumulation (encompassing all scales) happens for 50 μm particles.

The level of accumulation can be quantified by the RDF, which is defined as the ratio of the number of particle pairs found at a given separation distance to the expected number in a nominally uniform suspension

$$\text{RDF}(r; t) = \frac{N_{\text{pairs}}/V_s}{N_i(N_i - 1)/2V_B},\tag{12}$$

where i indicates a particular particle size and N_{pairs} is the total number of pairs detected with a separation distance (r) falling in a spherical shell of inner radius equal to $R - \delta$ and outer radius
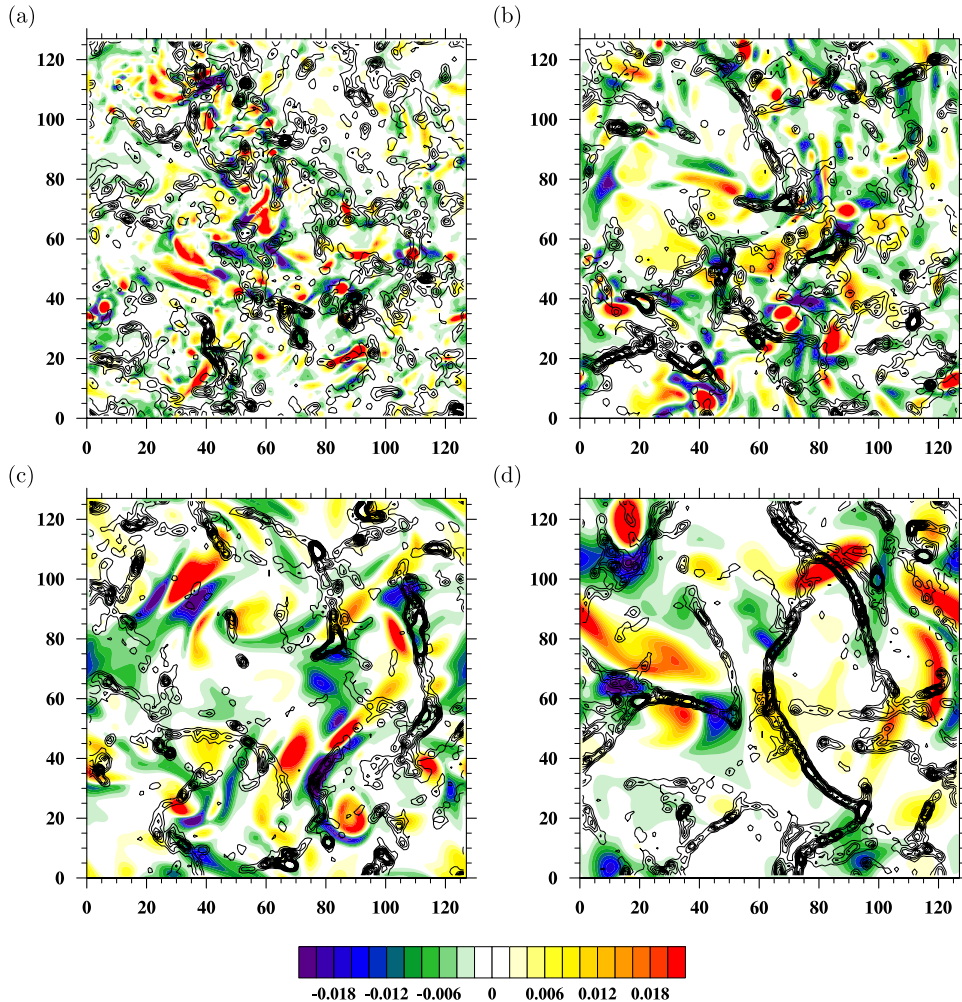
FIG. 14. Same as in Figure 12 but for particles with Stokes number 1.585 (droplet radius a = 50 μm). Different panels correspond to simulations performed with different forcing time scales (a) $t^* = 1$, (b) $t^* = 100$, (c) $t^* = 1000$, and (d) $t^* = 10\,000$.

equal to $R + \delta$. Here, δ is a small fraction (1%) of $R = 2a$.[31] V_s is the volume of the spherical shell, $V_s = 4\pi[(R + \delta)^3 - (R - \delta)^3]/3$. N_i is the total number of a_i droplets used in the simulation, and V_B is the volume of computational domain. RDF$(r;t)$ is further averaged over time to obtain RDF$(r = R)$. It is important to note that this RDF only quantifies the level of accumulation at the scale of collision radius, not all scales visualized in Figs. 12–14.

In this study, we compute the RDF using recently developed two-step algorithm[1] which minimizes numerical uncertainties. Figure 16 shows the RDF at contact ($r = R$) as a function of the Stokes number and particle size for the two different grid resolutions (128^3 and 256^3). In both simulations, we observe a similar trend. The RDF increases very quickly with particle radius for $a \le 30$ μm ($St \approx 0.5$) and then saturates. This initial rapid increase is due to the increase of droplet Stokes number. The observation is consistent with the visualizations presented in Figures 12 and 13. The saturation of accumulation at the scale of collision radius for $St > 0.5$ is a combined result of gravitational sedimentation and inertia. When the gravity is included, the settling droplets accumulate in the downward flow regions forming elongated (filament-like) structures (see Figure 15), but these structures have a length scale larger than the collision radius thus do not contribute significantly to the RDF here. We should emphasize that the saturation of the RDF here concerns nearly touching droplets i.e., at a separation $r = R$. Figure 16 does not reflect accumulation at larger
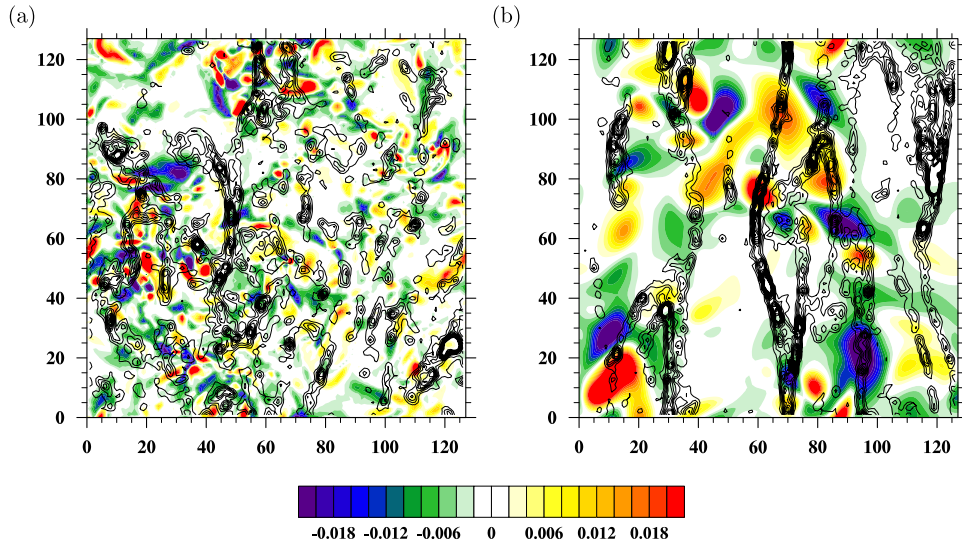
FIG. 15. Same as in Figure 14 ($St = 1.585$, droplet radius a $= 50$ μm) but for a vertical cross-section. Different panels correspond to simulations performed with different forcing time scales (a) $t^* = 1$ and (b) $t^* = 10\,000$.

separation distances. The elongated structures are stable and remain for a long time because the gravitational settling dominates the mechanism of turbulent mixing. This may be explained by the fact that gravity reduces the interaction time of particles with intermittent eddies. The stability of such structures tends to maintain the relative distance between droplets and hence the saturation of the RDF. This effect was discussed in detail by Rosa *et al*.[1] Gravity-driven clustering of inertial particles is also documented in other independent studies.[33,34]

The RDF computed in simulations with larger grid resolutions (256^3) takes somewhat larger values (except when the forcing time scale is very large $t^* = 10\,000$). The difference is greater for particles with larger inertia and this results from larger R_λ. The dependence on the Taylor microscale flow Reynolds number is consistent with observations reported in other studies.[1,31,35,36]

Sensitivity of the kinematic statistics on t_f is lower for smaller Stokes numbers. For larger Stokes numbers, the data points show significant statistical scatter. We conclude that for $St < 0.5$, the RDF takes greater values for longer forcing time scales. For a very long t^* such as $t^* = 10\,000$, the shape of the RDF is visibly different: first, the RDF has an apparent maximum; second, for the small droplets $a \le 30$ μm the values of RDF are greater (than for the other simulations with a shorter t_f) while for larger particle $a > 30$ μm the values are smaller. We note that, for a given particle size, there is a finite range of flow length scales that contribute to particle accumulation and the RDF. Outside this range, turbulent motion mixes the particles and erases the accumulation. Gravity affects the interaction time of inertial particles with an eddy. Consequently, the RDF tends to be larger for small-size droplets as the large-scale mixing homogenization is limited when t_f is large. On the other hand, for large-size droplets, the lack of large-scale eddies implies that the gravitational effect is stronger leading to insufficient time for the droplets to interact with small eddies, thus unable to cause a large RDF. We must stress again here that the RDF mainly measures accumulation at small scales.

To be complete, we also present in Figure 16 the RDF computed using deterministic forcing.[10,11] Apart from the simulations performed with very large forcing time scale ($t^* = 10\,000$), the radial distribution functions computed using different forcing methods are in quantitative agreement if $St < 0.5$. The difference between deterministic and stochastic schemes appears for particles with larger inertia ($St > 0.5$). This can be explained by the fact that the particles with larger inertia interact with a wider range of turbulent scales and some of the scales (these corresponding to low wave numbers) can be influenced by the forcing method. The flow forced with deterministic scheme has a larger Taylor microscale flow Reynolds number at the same mesh size. This implies that the flow under the deterministic forcing contains a slightly wider range of flow length scales leading to a slightly different RDF. For the two resolutions 128^3 and 256^3, we obtained $R_\lambda = 120.9$ and $R_\lambda = 196.9$, respectively.
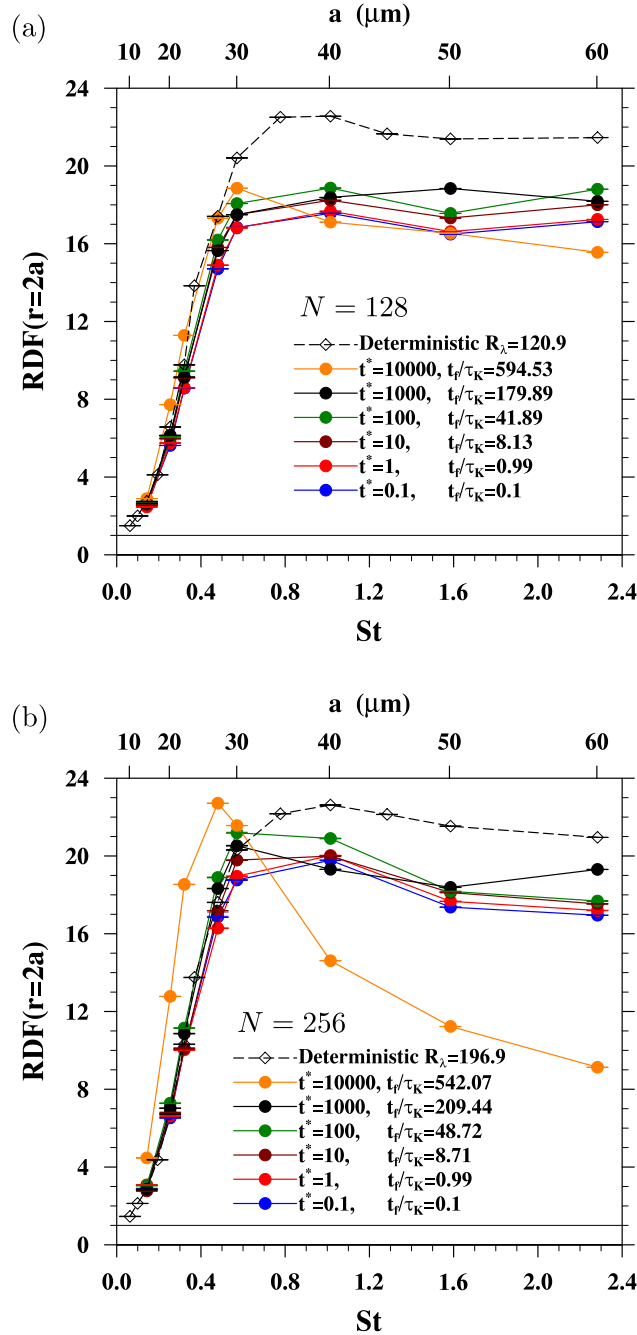
FIG. 16. Radial distribution function at contact ($r = 2a$) as a function of droplet Stokes number and radius obtained in simulations with two different grid sizes (a) 128^3 and (b) 256^3. Different colors correspond to simulations with different forcing time scales. Energy dissipation rate was set to $\epsilon = 400$ cm^2 s^{-3}. Dashed line represents results from DNS performed with deterministic forcing scheme.[1] The black solid lines at RDF($2a$) = 1 refer to a uniform particle concentration.

The values of R_λ for the stochastic forcing are about 30% lower (at shorter time scale), namely, $R_\lambda = 86$ at 128^3 and $R_\lambda = 145$ at 256^3.

The radial relative velocity w_r is defined in terms of the relative velocity **w** between two droplets with the separation vector **r** as $w_r = \mathbf{w} \cdot \mathbf{r}/|\mathbf{r}|$. The methodology for computing w_r between particles is similar to that described by Rosa *et al.*[1] Figure 17 presents the monodisperse w_r of nearly touching particles as a function of the particle radii for two different resolutions (128^3 and 256^3).
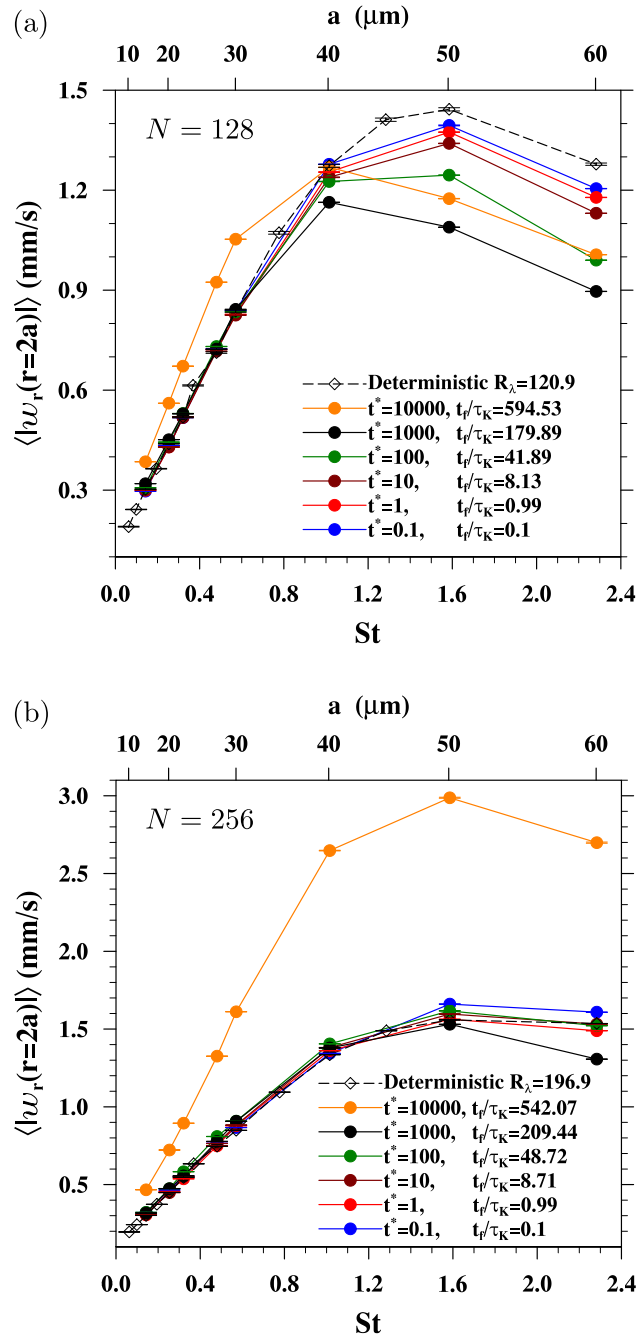
FIG. 17. Radial relative velocity of settling particles at contact ($r = 2a$) as a function of droplet radius obtained in simulations with two different grid sizes (a) 128^3 and (b) 256^3. Similarly, as in Figure 16, different colors correspond to simulations with different forcing time scales. For comparison, data from simulations with a deterministic scheme have been added (black dashed line).

Several observations can be made from Figure 17. For small particles $a \leq 30$ μm, the relative velocity increases monotonically with the particle size. It is due to increasing contributions from larger scale of turbulent motion and increasing nonlocal effects (e.g., caustics). All the results (except that one for $t^* = 10\,000$) collapse to the same curve. For larger particles $a > 30$ μm, the gravity gradually diminishes the effect of turbulent motion due to shorter droplet-eddy interaction time, leading to slowly decreasing w_r with increasing droplet size. For this range ($a > 30$ μm), we

observe a noticeable dependence of w_r on the forcing time scale. The dependence results from the varying range of scales present in the turbulent flow. Simulations with shorter time scales yield higher values of relative velocity due to a wider range of scales in the flow. Similarly, as for the radial distribution function, the statistics of w_r obtained in simulations with very long time scale $t^* = 10\,000$ are very different than others obtained with shorter time scales. The values of w_r are larger (especially at resolution 256^3), which could be due to a higher energy level of the far inertial subrange and dissipation-range eddies (see, for example, Figures 4 and 5).

V. KINEMATIC AND DYNAMIC STATISTICS FOR INERTIAL PARTICLES CONDITIONED ON LOCAL ENSTROPHY AND ENERGY DISSIPATION RATE

The three-dimensional vorticity fields presented in Figure 1 show that different forcing time scales result in different flow structures. To further elucidate the correlation between the altered flow structures and dynamics of suspended inertial particles, a conditional analysis has been performed. Conditional statistics are a convenient tool which greatly facilitates the analysis and have been employed frequently in other studies[21,36–38] to extract information on the coupling between a fluid and a set of Lagrangian particles. Here, we present a series of results illustrating the two-point statistics conditioned on the local enstrophy $\Omega = 0.5|\bar{\omega}|^2$ and the energy dissipation rate.

The statistics were computed using the method proposed by Wang and Maxey.[24] First, we evolved the flow (grid size 128^3) with particles up to $120\,000$ time steps (16.9-$94.7T_e$ depends on t^*). This time was necessary and sufficient to reach a statistically stationary state of the monodisperse systems. The number of particles in each simulation depends on the volume fraction and ranges between $90\,000$-$400\,000$. The collision and flow statistics were collected during $280\,000$ successive time steps. Due to the large amounts of data, the statistics were computed on the fly. The time period ($280\,000$ time steps) used for the data collection expressed in eddy turnover time corresponds to $224T_e$ for the shortest forcing time scale (0.1) and $40T_e$ for the forcing time $t^* = 10\,000$.

The data presented in Figure 18 were computed as follows. The normalized enstrophy Ω/Ω_{max} was divided into one of $m = 300$ bins $(i - 1) \leq m \cdot \Omega/\Omega_{max} < i$, $i = 1, 2, \ldots, m$. Then, all the 128^3 grid points at each time steps were scanned to find the number of grid points, where the value of enstrophy fell into the range for the i-th slot. At the post-processing stage, the data were normalized to determine the probability density function PDF(Ω). At the same time, we counted number of colliding pairs at each enstrophy level. The algorithm for collision detection follows the idea
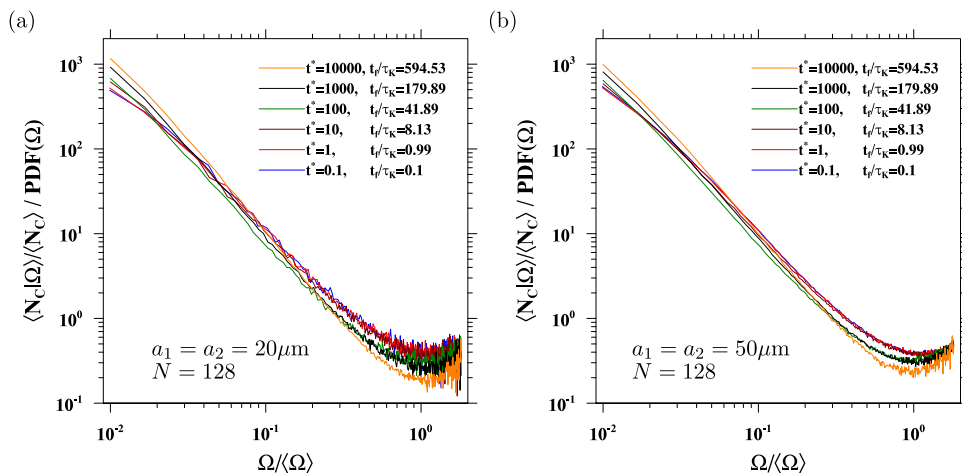

FIG. 18. Correlation between the local collision rate and enstrophy as a function of normalized enstrophy. Series of simulations were performed for two monodisperse systems with (a) 20 μm and (b) 50 μm droplets. $\langle N_C|\Omega \rangle$ defines conditional expectation of the number density (collisions). $\langle N_C \rangle$ is the average collision rate. PDF(Ω) refers to probability density function of the fluid enstrophy. Normalization by PDF is required since different enstrophy occupy different amount of physical space.
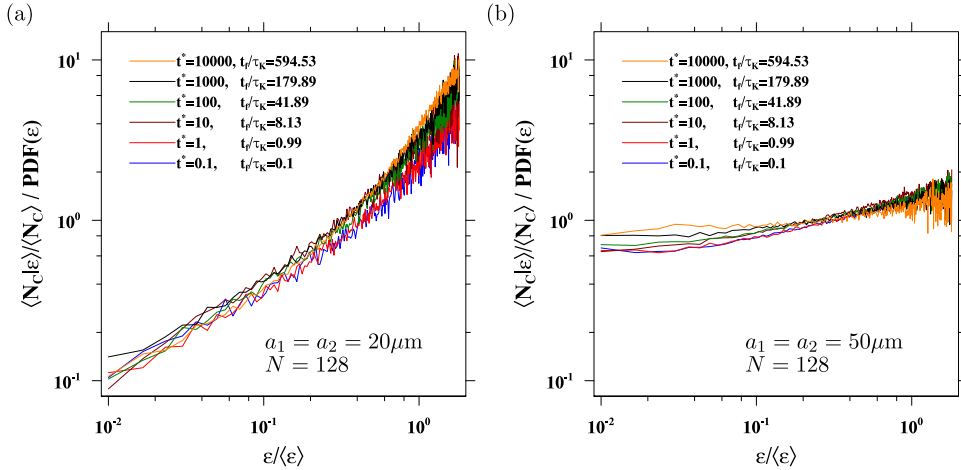
FIG. 19. Correlation between the local collision rate and energy dissipation rate as a function of normalized energy dissipation rate. Panel (a) monodisperse systems with 20 μm droplets; (b) monodisperse systems with 50 μm droplets.

presented by Wang *et al.*,[39] with several modifications resulting from different memory management in the MPI code. The conditionally averaged concentration of colliding pairs is defined as $\langle N_C|\Omega\rangle/\langle N_C\rangle/\text{PDF}(\Omega)$ where $\langle N_C|\Omega\rangle/\langle N_C\rangle$ is the conditional expectation of the number density of colliding pairs normalized by the field mean.

A similar analysis has been performed for collision statistics conditioned on the local energy dissipation rate. Figure 19 shows correlation between the local collision rate and energy dissipation rate as a function of normalized energy dissipation rate.

Figures 18 and 19 demonstrate that the collision statistics computed with different forcing time scales are actually quite similar. Figure 18 indicates that there is no qualitative difference between the simulations performed with different droplet sizes. Our results are consistent with the observations made in Wang and Maxey.[24] The regions of higher collision rate are well correlated with the regions of lower vorticity. Interestingly, the conditional statistics saturate at $\Omega = \langle\Omega\rangle$ and then increase for very large Ω. The increases at very large Ω may result from non-local dynamics of inertial particles. Some collisions occur between particles approaching from large separations. Such particles experience more energetic turbulence and can collide in regions where Ω is relatively large. A different trend is observed in collision statistics related to the local energy dissipation rate.
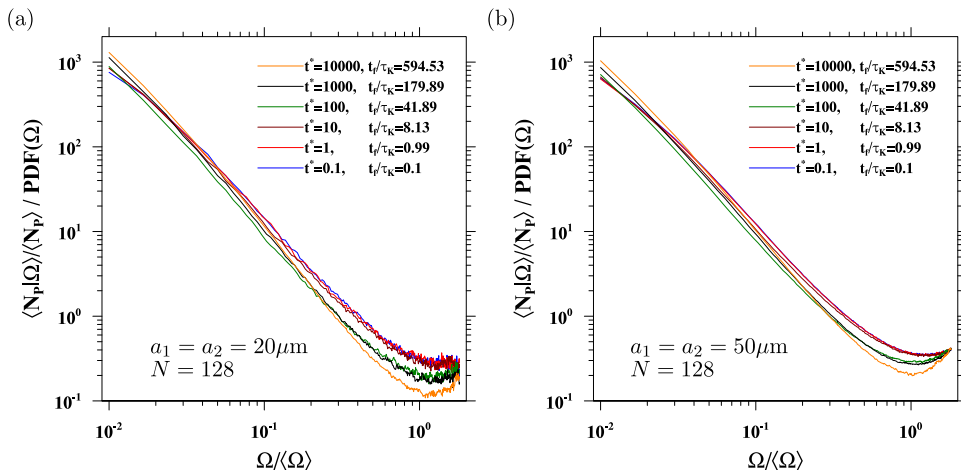

FIG. 20. Statistics as in Figure 18 but for nearly touching droplets. Panel (a) monodisperse systems with 20 μm droplets; (b) monodisperse systems with 50 μm droplets.
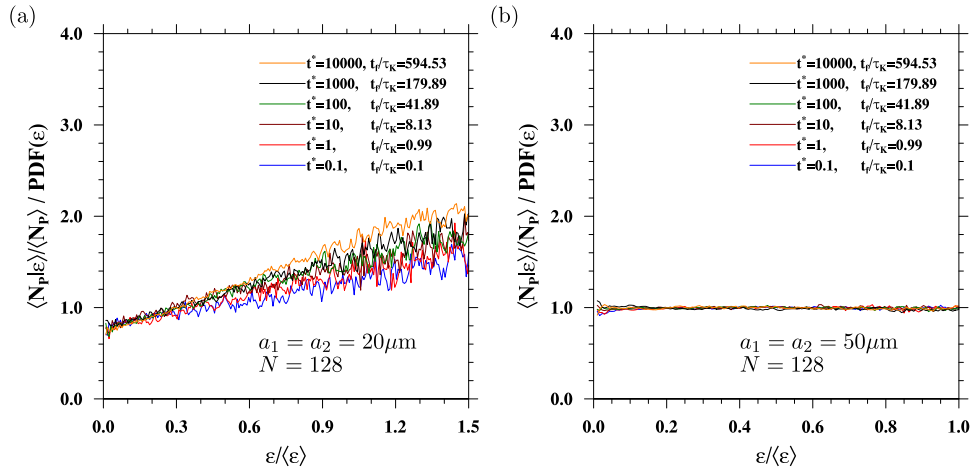
FIG. 21. Statistics as in Figure 19 but for nearly touching droplets. Panel (a) monodisperse systems with 20 μm droplets; (b) monodisperse systems with 50 μm droplets.

Figure 19(a) shows that for 20 μm droplets the regions with higher collision rate are correlated with the region of high energy dissipation rate. However, for larger droplets (50 μm), the spatial distribution of collision events corresponds closely to PDF(ϵ) of the flow. Hence, the correlation factor is close to 1. This is due to the fact that the larger particles show a weaker tendency to accumulate in regions of high energy dissipation rate. This mechanism is illustrated in Figure 15.

The next analysis concerns the probability of detecting pairs with a separation distance close to geometric collision radius (nearly touching particles) ($2a - \delta < |r| < 2a + \delta$). Here, δ is a small fraction of particle radius (2%). The statistics of nearly touching particles were conditioned on the local enstrophy and energy dissipation. Again the focus is only on the monodisperse systems. Figures 20 and 21 show conditional statistics of nearly touching pairs of size (a) $a = 20$ μm and (b) $a = 50$ μm. The current analysis and the previous one concerning colliding particles are inter-related. It stems from the fact that the local collision rates are proportional to the second moment of local droplet concentrations.[2]

Figures 20 and 21 demonstrate a good agreement of simulation results with different forcing time scales. We conclude that the forcing time scale does not significantly affect these conditional statistics. The only difference is seen in $\langle N_P | \epsilon \rangle / \langle N_P \rangle / \text{PDF}(\epsilon)$. For nearly touching particles, the correlation is less sensitive to ϵ than for colliding pairs (see Figure 19(a)).

To compute the conditional statistics, we faced with the problem of computing energy dissipation rate in the real space. The standard formula for dissipation rate[40] $2\mu e_{ij}^2$ includes partial derivatives terms $\partial u_i / \partial x_j$. In our code, these terms were computed in the Fourier space and transferred to the real space using inverse parallel FFT.

VI. CONCLUSIONS

Using direct numerical simulations, we have examined the effects of the forcing time scale t_f on the characteristics of the forced turbulent flows. The numerical simulations were developed employing the well-known random forcing method developed by Eswaran and Pope.[12] The main focus was on the relationship between the forcing time scales and the vortical structures of turbulent flows. A number of statistics characterizing the turbulent flow, such as R_λ, integral length scale, flatness, and skewness, have been computed and analyzed. Also, effects of the forcing time scale on the kinematic collision statistics of inertial particles have been investigated. The results provide insights into simulations of forced turbulence and its applications.

A large number of simulations were performed with our new parallel implementation based on two-dimensional domain decomposition.[18] The energy spectra of the simulated flows computed with different forcing time scales and at different grid resolutions are found to be consistent with

experimental data, i.e., the energy spectra of grid generated turbulence in wind tunnel. The probability density functions for the normalized vorticity obtained with different forcing time scales differ only in the tails. We argue that these differences result mainly from different flow Reynolds numbers. The size of vortical structures at small scales increases with increasing t_f. The energy dissipation rate obtained in the numerical simulations agrees well with the analytical formula of Eswaran and Pope[12] using $\beta = 0.8$. However, for very small time scales, $\beta = 1.5$ was found to yield a better agreement between theory and DNS results. Energy dissipation rate remains constant for any t_f smaller than τ_K or $t_f < 0.1T_e$. Similar conclusions can be drawn for the other flow statistics. Taylor microscale flow Reynolds number, integral length scale, skewness, and flatness do not change if $t_f \leq \tau_K$. For large forcing time scales, the skewness and flatness show a strong dependence on the t_f, which could be a result of very low flow Reynolds numbers.

In a series of simulations, we investigated the effects of forcing time scale on the kinematic collision statistics. The RDF does not reveal significant differences if $t^* \leq 1000$. As expected, these differences are greater for heavier particles. Interestingly, for very large forcing scales $t^* = 10\,000$, the differences in the RDF become important. It should be emphasized that the magnitude of these differences depends much on the domain size and thus on R_λ.

Results of the kinematic collision statistics (RDF and relative velocity) obtained with stochastic forcing scheme have been compared to the analogous statistics computed with deterministic forcing. Simulations performed with different forcing methods give the same kinematic statistics for small inertia particles ($St < 0.5$). The only exception are simulations performed with the very long forcing time scale ($t^* = 10\,000$). The effect of the forcing method becomes clear for the particles with larger inertia and especially in the RDF. For larger particles ($a > 25\,\mu$m), the RDF computed with deterministic scheme is about 15% greater. Radial relative velocity is less sensitive to the forcing mechanism. Simulations at the 128^3 resolution show that the difference in the radial relative velocity computed with different forcing methods becomes smaller as t^* decreases. For simulations at higher resolution (256^3), the statistics of w_r are in the quantitative agreement.

In general, the results show that the RDF and radial relative velocity may depend on the forcing time scale if it becomes large. This dependence, however, can be largely explained in terms of the altered flow Reynolds number and the changing range of flow length scales present in the turbulent flow. We conclude that both flow statistics and particles kinematic statistics are not sensitive to the forcing time scales if the scales are smaller than τ_K. To avoid the undesirable dependency on t_f, we suggest to set the forcing time scales as $dt \leq t_f \leq \tau_K$.

Finally, conditional statistics have been obtained. We analyzed two-point statistics conditioned on the local enstrophy and the energy dissipation rate. We found that the regions of higher collision rate are well correlated with the regions of lower vorticity. Regions of higher concentration of pairs at contact are highly correlated with the region of high energy dissipation rate. The normalized conditional statistics computed with different forcing time scales appear to be very similar, but they depend nonlinearly on the particle size, local flow vorticity, and dissipation rate.

[1] B. Rosa, H. Parishani, O. Ayala, W. W. Grabowski, and L.-P. Wang, "Kinematic and dynamic collision statistics of cloud droplets from high-resolution simulations," New J. Phys. **15**, 045023 (2013).

[2] W. W. Grabowski and L.-P. Wang, "Growth of cloud droplets in a turbulent environment," Annu. Rev. Fluid Mech. **45**, 293-321 (2013).

[3] L.-P. Wang, B. Rosa, H. Gao, G. W. He, and G. D. Jin, "Turbulent collision of inertial particles: Point-particle based, hybrid simulations and beyond," Int. J. Multiphase Flow **35**, 854-867 (2009).

[4] J. Chun, D. Koch, S. L. Rani, A. Ahluwalia, and L. R. Collins, "Clustering of aerosol particles in isotropic turbulence," J. Fluid Mech. **536**, 219-251 (2005).

[5] M. Ulitsky, C. Ghenai, I. Gokalp, L.-P. Wang, and L. Collins, "A comparison of a spectral EDQNM model for premixed turbulent flame propagation to DNS and experiments," Combust. Theory Modell. **4**(3), 241-264 (2000).

[6] V. Eswaran and S. B. Pope, "Direct numerical simulations of the turbulent mixing of a passive scalar," Phys. Fluids **31**, 506 (1988).

[7] A. Juneja and S. B. Pope, "A DNS study of turbulent mixing of two passive scalars," Phys. Fluids **8**, 2161-2184 (1996).

[8] T. Ishihara, T. Gotoh, and Y. Kaneda, "Study of high-Reynolds number isotropic turbulence by direct numerical simulation," Annu. Rev. Fluid Mech. **41**, 165-180 (2009).

[9] G. S. Patterson and S. A. Orszag, "Spectral calculations of isotropic turbulence: Efficient removal of aliasing interactions," Phys. Fluids **14**, 2538-2541 (1971).

[10] N. P. Sullivan, S. Mahalingam, and R. M. Kerr, "Deterministic forcing of homogeneous isotropic turbulence," Phys. Fluids **6**, 1612-1614 (1994).

[11] S. Chen and X. Shan, "High-resolution turbulence simulations using the connection machine-2," Comput. Phys. **6**(6), 643-646 (1992).

[12] V. Eswaran and S. B. Pope, "An examination of forcing in direct numerical simulations of turbulence," Comput. Fluids **16**, 257-278 (1988).

[13] S. Balachandar and J. K. Eaton, "Turbulent dispersed multihase flow," Annu. Rev. Fluid Mech. **42**, 111-133 (2010).

[14] O. Ayala, W. W. Grabowski, and L.-P. Wang, "A hybrid approach for simulating turbulent collisions of hydrodynamically-interacting particles," J. Comput. Phys. **225**, 51-73 (2007).

[15] S. A. Orszag and G. S. Patterson, "Numerical simulation of three-dimensional homogeneous isotropic turbulence," Phys. Rev. Lett. **28**(2), 76-79 (1972).

[16] M. P. Allen and D. J. Tildesley, *Computer Simulation of Liquids* (Oxford University Press, 1987).

[17] O. Ayala and L.-P. Wang, "Parallel implementation and scalability analysis of 3D fast Fourier transform using 2D domain decomposition," Parallel Comput. **39**, 58-77 (2013).

[18] O. Ayala, H. Parishani, L. Chen, B. Rosa, and L.-P. Wang, "DNS of hydrodynamically interacting droplets in turbulent clouds: Parallel implementation and scalability analysis using 2D domain decomposition," Comput. Phys. Commun. **185**, 3269-3290 (2014).

[19] S. B. Pope, *Turbulent Flows* (Cambridge University Press, Cambridge, New York, 2000).

[20] M. R. Maxey and J. J. Riley, "Equation of motion for a small rigid sphere in a nonuniform flow," Phys. Fluids **26**, 883-889 (1983).

[21] K. D. Squires and J. K. Eaton, "Particle response and turbulence modification in isotropic turbulence," Phys. Fluids **2**, 1191-1203 (1990).

[22] F. Moisy and J. Jimenez, "Geometry and clustering of intense structures in isotropic turbulence," J. Fluid Mech. **513**, 111-133 (2004).

[23] G. Comte-Bellot and S. Corrsin, "Simple Eulerian time correlation of full- and narrow-band velocity signals in grid-generated, 'isotropic' turbulence," J. Fluid Mech. **48**, 273-337 (1971).

[24] L.-P. Wang and M. R. Maxey, "Settling velocity and concentration distribution of heavy particles in a forced isotropic and homogeneous turbulence," J. Fluid Mech. **256**, 27-68 (1993).

[25] K. R. Sreenivasan, "On the universality of the Kolmogorov constant," Phys. Fluids **7**, 2778-2784 (1995).

[26] J. O. Hinze, *Turbulence* (McGraw-Hill, New York, 1975).

[27] H. Tennekes and J. L. Lumley, *A First Course in Turbulence* (MIT press, Cambridge, Massachusetts, 1972).

[28] T. Ishihara, Y. Kaneda, M. Yokokawa, K. Itakura, and A. Uno, "Small-scale statistics in high-resolution direct numerical simulation of one point velocity gradient statistics," J. Fluid Mech. **592**, 335-366 (2007).

[29] H. Parishani, O. Ayala, B. Rosa, and L.-P. Wang, "Effects of gravity on the inertial-particle acceleration and radial relative velocity in homogeneous isotropic turbulence," personal communication (2015).

[30] O. Ayala, B. Rosa, L.-P. Wang, and W. W. Grabowski, "Effects of turbulence on the geometric collision rate of sedimenting droplets: Part 1. Results from direct numerical simulation," New J. Phys. **10**, 075015 (2008).

[31] L.-P. Wang, A. S. Wexler, and Y. Zhou, "Statistical mechanical descriptions of turbulent coagulation of inertial particles," J. Fluid Mech. **415**, 117-153 (2000).

[32] E. J. P. Woittiez, H. J. J. Jonker, and L. M. Portela, "On the combined effects of turbulence and gravity on droplet collisions in clouds: A numerical study," J. Atmos. Sci. **66**, 1926-1943 (2009).

[33] Y. Park and C. Lee, "Gravity-driven clustering of inertial particles in turbulence," Phys. Rev. E **89**, 061004(R) (2014).

[34] R. J. Hill, "Geometric collision rates and trajectories of cloud droplets falling into a Burger vortex," Phys. Fluids **17**, 037103 (2005).

[35] R. Onishi, K. Takahashi, and J. S. Vassilicos, "An efficient parallel simulation of interacting inertial particles inhomogeneous isotropic turbulence," J. Comput. Phys. **242**, 809-827 (2013).

[36] R. Onishi and J. S. Vassilicos, "Collision statistics of inertial particles in two-dimensional homogeneous isotropic turbulence with an inverse cascade," J. Fluid Mech. **745**, 279-299 (2014).

[37] V. Dallas and J. C. Vassilicos, "Rapid growth of cloud droplets by turbulence," Phys. Rev. E **84**, 046315 (2011).

[38] V. E. Perrin and H. J. J. Jonker, "Preferred location of droplet collisions in turbulent flows," Phys. Rev. E **89**, 033005 (2014).

[39] L.-P. Wang, C. N. Franklin, O. Ayala, and W. W. Grabowski, "Probability distributions of angle of approach and relative velocity for colliding droplets in a turbulent flow," J. Atmos. Sci. **63**, 881-900 (2006).

[40] S. Chandrasekhar, *Hydrodynamic and Hydromagnetic Stability* (Dover edition, 1961).